



Crustal structure determined from ambient noise tomography near the magmatic centers of the Coso region, southeastern California

Yingjie Yang

Center for Imaging the Earth's Interior, Department of Physics, University of Colorado at Boulder, Boulder, Colorado 80309, USA

Now at GEMOC ARC National Key Centre, Department of Earth and Planetary Sciences, Macquarie University, Sydney, NSW 2109, Australia (yingjie.yang@mq.edu.au)

Michael H. Ritzwoller

Center for Imaging the Earth's Interior, Department of Physics, University of Colorado at Boulder, Boulder, Colorado 80309, USA

Craig H. Jones

Department of Geological Sciences, University of Colorado at Boulder, Boulder, Colorado 80309, USA

[1] We apply seismic ambient noise tomography to image and investigate the shallow shear velocity structure beneath the Coso geothermal field and surrounding areas. Data from a PASSCAL experiment operated within the Coso geothermal field between 1998 and 2000 and surrounding broadband stations from the Southern California Seismic Network are acquired and processed. Daily cross correlations of ambient noise between all pairs of stations that overlapped in time of deployment were calculated and then stacked over the duration of deployment. Phase velocities of Rayleigh waves between 3 and 10 s periods are measured from the resulting cross correlations. Depending on the period, between about 300 and 600 reliable phase velocity measurements are inverted for phase velocity maps from 3 to 10 s periods, which in turn are inverted for a 3-D shear velocity model beneath the region. The resulting 3-D model reveals features throughout the region that correlate with surface geology. Beneath the Coso geothermal area shear velocities are generally depressed, a prominent low-velocity anomaly is resolved clearly within the top 2 km, no significant anomaly is seen below about 14 km depth, and a weakly resolved anomaly is observed between 6 and 12 km depth. The anomaly in the top 2 km probably results from geothermal alteration in the shallow subsurface, no magmatic body is imaged beneath 14 km depth, but the shear velocity anomaly between 6 and 12 km may be attributable to partial melt. The thickness and amplitude of the magma body trade off in the inversion and are ill determined. Low velocities in the regions surrounding Coso at depths near 7 km underlie areas with Miocene to recent volcanism, suggesting that some magmatic processing of the crust could be focused near this depth.

Components: 9200 words, 16 figures, 1 table.

Keywords: Coso geothermal area; ambient noise; surface wave tomography.

Index Terms: 7280 Seismology: Volcano seismology (4302, 8419); 7255 Seismology: Surface waves and free oscillations.

Received 14 September 2010; **Revised** 28 December 2010; **Accepted** 4 January 2011; **Published** 19 February 2011.

Yang, Y., M. H. Ritzwoller, and C. H. Jones (2011), Crustal structure determined from ambient noise tomography near the magmatic centers of the Coso region, southeastern California, *Geochem. Geophys. Geosyst.*, 12, Q02009, doi:10.1029/2010GC003362.

1. Introduction

[2] The Coso geothermal area lies at the southwestern corner of the actively deforming part of the basin and range and within the Eastern California Shear Zone. This region is unusual in apparently accommodating westward motion of the Sierra Nevada through a complex combination of surficial normal, thrust, and strike-slip faulting as well as vertical axis rotation [e.g., Jones, 1987; Hauksson and Unruh, 2007; Taylor et al., 2008; Pluhar et al., 2006]. It also lies in the last part of the basin and range to experience significant volcanism [e.g., Armstrong and Ward, 1991; McQuarrie and Oskin, 2010]. The Coso Range contains one of the young magmatic centers along the western margin of the basin and range that originated about 4 Ma but entered a phase of bimodal volcanism about 1 Ma [Duffield et al., 1980]. Among the more intriguing suggestions has been that the Coso geothermal area overlies an emerging core complex representing rising lower crustal rock with an associated magmatic system [Monastero et al., 2005].

[3] An exceptionally diverse collection of geophysical and geological analyses have been applied to the Coso geothermal area and surroundings, largely in an attempt to characterize the geothermal resource being exploited for the generation of electricity. Much of the work characterizes the uppermost few kilometers of the crust, including active source refraction and reflection profiling [Pullammanappalil et al., 2001; Unruh et al., 2008], local earthquake source characteristics [Feng and Lees, 1998; Hough et al., 1999; Bhattacharyya et al., 1999; Bhattacharyya and Lees, 2002; Hauksson and Unruh, 2007], seismic velocity tomography from local earthquakes [Walck and Clayton, 1987; Walck, 1988; Wu and Lees, 1999; Lees and Wu, 2000; Hauksson and Unruh, 2007], magnetotellurics [Newman et al., 2008], seismic attenuation tomography [Young and Ward, 1980; Sanders et al., 1988; Wu and Lees, 1996; Hough et al., 1999], and surface heat flow [Combs, 1980]. The overall picture of the region from these works is of a complex brittlely deforming crust above ~4 km depth in the vicinity of the geothermal area, with brittle failure extending to 8–12 km depth in the surrounding area.

[4] Deeper variations in structure have been probed less frequently, in part because of the complications near the surface, in part because of the absence of deeper local seismicity, and in part because of the focus on shallow structure relevant to geothermal

exploration. Within the Coso geothermal area, two main questions have emerged: the depth of the magma chamber(s) acting as the heat source and the relationship of magmatism to faulting or shearing at depth. Three main studies bear on the structure of the Coso geothermal field below 5 km depth: a teleseismic receiver function study by Wilson et al. [2003], a regional and local earthquake travel time tomography study by Hauksson and Unruh [2007] and an active source reflection profile by Unruh et al. [2008]. Both the receiver function and reflection profile experiments observe a strong seismic converter/reflector at about 5 km depth. Wilson et al. [2003] interpreted this as the top of the magma chamber containing at least 1.5% melt, an interpretation consistent with a petrological analysis by Manley and Bacon [2000]. Hauksson and Unruh [2007], in contrast, infer from V_p/V_s ratios that the volume between about 5 and 10 km depth cannot contain melt. In their interpretation, the magma chamber is below ~10 km, under a deeper reflector seen by Unruh et al. [2008]. Hauksson and Unruh [2007] suggest that the discrepancy with Wilson et al. [2003] resulted from the limited vertical resolution of vertical rays. Receiver functions, however, do provide good vertical resolution but are insensitive to small gradients in wave speeds. An alternative explanation for the discrepancy is the lack of horizontal resolution in the local earthquake tomography both because of the absence of local earthquakes within or beneath the purported magma chamber and because of raybending around extreme low-velocity bodies. In any event, the depth of any magma chamber and the ultimate source of the heat for the geothermal field remains disputed.

[5] In the past few years, novel interferometric methods of seismic imaging based on ambient noise have been developed. Methods based on ambient noise, called “ambient noise tomography” (ANT), have proven effective [Shapiro et al., 2005; Sabra et al., 2005] at extracting short-period (6–30 s) surface waves from ambient seismic noise to constrain structures in the middle to lower crust and the uppermost mantle. Ambient noise tomography is based on cross correlations of long recordings of seismic noise observed between pairs of stations to construct surface wave dispersion measurements at short and intermediate periods. Previous studies based on ambient noise tomography have been applied mostly at regional scales including in New Zealand [Lin et al., 2007], Southern Africa [Yang et al., 2008a], Spain [Villaseñor et al., 2007], Korea [Cho et al., 2007], Japan [Nishida et al., 2008], Tibet [e.g., Yao et al., 2006], and the western U.S.

[6] *Moschetti et al.* 2007, 2010a, 2010b; *Lin et al.*, 2008; *Yang et al.*, 2008b; *Lin et al.*, 2010] but also at continental scales across Europe [*Yang et al.*, 2007], China [*Zheng et al.*, 2008; *Yang et al.*, 2010], the USA [*Bensen et al.*, 2008, 2009], and Australia [*Saygin and Kennett*, 2010].

[6] In this study, we apply ambient noise tomography at a subregional scale with an aperture of ~200 km to image shallow V_s structures beneath the Coso geothermal area and surrounding areas. The purpose is to attempt to constrain the depth of any magma chambers underlying the area using ambient noise dispersion measurements. To improve resolution of the shallow crust ambient noise dispersion measurements are extended down to 3 s periods. The relatively narrow aperture of the study, however, prohibits extending measurements above about 10 s periods.

2. Data and Methods

[7] Twenty subarrays of the Coso PASSCAL experiment, composed of both short-period and broadband instruments, were deployed in and near the Coso geothermal area from November 1998 to May 2000 [e.g., *Wilson et al.*, 2003]. These 20 subarrays had numerous overlaps in time of deployment, which results in many interstation raypaths between coeval subarrays. Overall, about 143 station sites were occupied in this experiment. Surrounding this PASSCAL experiment, there are about 67 seismic stations from the Southern California Seismic Network (SCSN), 30 equipped with broadband sensors and the rest equipped with short-period sensors. Continuous data since 1998 from 20 of these SCSN stations are archived at the IRIS/DMC, which allows us to obtain cross correlations between the stations of the Coso PASSCAL experiment and the SCSN stations. Data recorded after January 2008 from the rest of the 67 SCSN seismic stations were acquired from the online data center at the Southern California Earthquake Center (SCEC). The locations of these stations are plotted in Figure 1.

[8] Even though some stations used in this study possess short-period sensors with a passband above 1 Hz, significant ambient noise energy can still be observed in the period range from 1 to 10 s. Figure 2 shows the spectra of ambient seismic noise recorded at several short-period (stations LBE1, LBTE5 and WHAE1) and broadband stations (stations MPM and WHA00). These spectra are quite similar between 0.1 and 1 Hz (1–10 s period) for both short-period and broadband stations. The largest ampli-

tudes are in the microseismic band between 0.1 and 0.2 Hz (5–10 s). Spectra decay gradually away from the microseismic band and tend to be nearly flat at frequencies higher than 0.2 Hz (periods <5 s). As demonstrated in section 3, surface waves at periods from 3 to 10 s can be extracted from cross correlations among the short-period stations, between short-period stations and broadband stations, or among the broadband stations.

[9] After accumulating continuous seismic data, we first check for possible errors in timing and polarization based on the first arrivals of earthquake waves (P waves). We find that several PASSCAL stations have timing errors, although no timing errors are found for the SCSN stations. The PASSCAL stations with timing errors are removed from the data set because there are nearby stations within each subarray. We also find that some short-period PASSCAL stations have inverse vertical polarities compared to broadband stations. Before further data processing, we invert the vertical time series of those stations to align them with the vertical polarity of the broadband stations.

[10] Most (but not all) short-period stations from the Coso PASSCAL network have glitches in the time domain while broadband stations are glitch-free. These glitches were typically generated by difficulties with the electronics of a preamplifier used to expand the frequency response of many of the instruments. Examples of seismograms with glitches and without glitches are plotted in Figure 3a. The amplitude, width and time interval of the glitches vary between stations. However, these glitches are typically at low frequencies, with large amplitudes mainly at periods between 50 and 100 s. After we apply a high-pass filter to the seismograms with a corner frequency at 0.1 Hz, glitches become much smaller (Figure 3b). To remove the effect of glitches more completely, we further apply a running-absolute-mean normalization. This normalization computes the running average of the absolute value of the waveform in a normalization time window of fixed length and weights the waveform at the center of the window by the inverse of this average. The width of the normalization we use here is 1 s. The running-absolute-mean normalization suppresses the amplitude of glitches to the same level as the ambient noise (Figure 3c).

[11] The data processing procedure applied here is very similar to that described in detail by *Bensen et al.* [2007, 2008] and *Lin et al.* [2008]. Using only the vertical component of ambient noise implies that the cross correlations we obtain predominantly

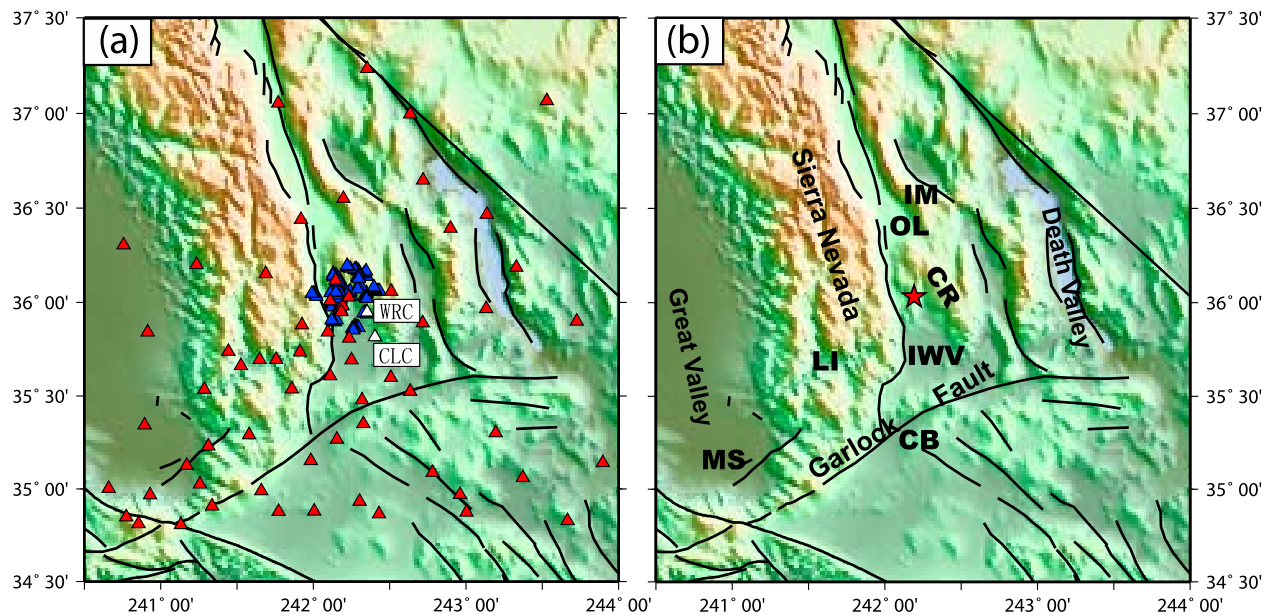


Figure 1. (a) Distribution of seismic stations in the Coso geothermal area and surrounding areas used in this study. There are 67 Southern California Seismic Network (SCSN) stations denoted by the red and white triangles with continuous data being archived by the Southern California Earthquake Data Center (SCEDC) since January 2008. The two white triangles show the locations of a broadband station CLC and a short-period station WRC. The blue triangles denote the Coso PASSCAL stations. Black lines denote faults. (b) Place names mentioned in text: CB, Cantil Basin; CR, Coso Range; IM, Inyo Mountains; IWV, Indian Wells Valley; LI, Lake Isabella; MS, Maricopa Subbasin; OL, Owens Lake.

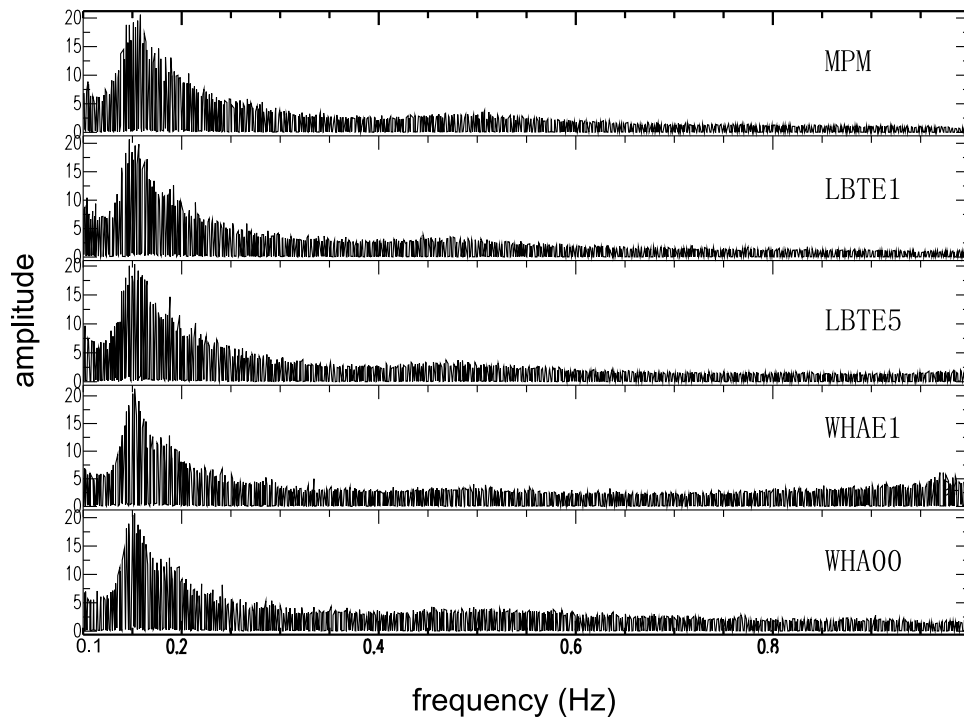


Figure 2. Examples of amplitude spectra between 0.1 and 1 Hz for daily ambient noise data from five stations (top to bottom): MPM, LBTE1, LBTE5, WHAE1, and WHA00. Station MPM is from the SCSN network, the other four are PASSCAL stations. Stations MPM and WHA00 are broadband stations, whereas stations LBTE1, LBTE5, and WHAE1 are short-period stations.

contain Rayleigh wave signals. Continuous data are decimated to ten samples per second and then filtered in the period band from 1 to 10 s. Instrument responses are removed from the continuous data because different types of seismic sensors are used among the stations. Because the amplitudes of ambient noise at ~ 6 s periods dominate the spectra (Figure 2), spectral whitening is applied to flatten spectra over the entire period band (1–10 s). Time domain normalization then is applied to suppress the influence of earthquake signals and other irregularities, such as the glitches observed in the seismograms from some Coso PASSCAL stations (Figure 3). After these processes are completed, cross correlations are performed daily in the period band from 1 to 10 s and then are stacked over the 15 month period between March 1999 and May 2000 for the Coso PASSCAL stations and the 20 SCSN stations. Over the 21 month period from January 2008 to September 2009, cross correlations are performed similarly between the 67 SCSN stations.

3. Results of Cross Correlations

[12] In this study, we aim to retrieve surface waves at periods from 1 to 10 s, which would provide good constraints on V_s from the surface to ~ 20 km depth. However, as discussed in section 2, spectra of ambient noise have large amplitudes in the microseismic band between 0.1 and 0.2 Hz (5–10 s) but decay rapidly at frequencies higher than 0.2 Hz (< 5 s) (Figure 2). As a result, the shortest period of surface waves extracted from cross correlations of ambient noise is 3 s. Figure 4 shows examples of 1 month cross correlations among the Coso PASSCAL stations filtered in two period bands: 1–3 s and 3–10 s. There are strong and coherent surface wave signals in the cross correlations at 3–10 s periods, but, at 1–3 s periods there are no clearly aligned surface wave signals and the cross correlations are much noisier. In a separate unpublished study, Y. Yang and M. H. Ritzwoller (Spectral characteristics of ambient seismic noise and coda waves at periods from 1 to 10 s, manuscript in preparation, 2011) showed that ambient noise between 1 and 3 s periods dominantly arises from the Pacific coast in the westernmost U.S. and these waves are strongly attenuated as they propagate inland. Consequently, in the Coso geothermal area the amplitude of ambient noise at 1–3 s periods is very low, which results in very weak surface wave signals in the cross correlations. In the cross-correlation analysis here, we focus on the period

band from 3 to 10 s, which allows us, ultimately, to constrain shear velocities in the subsurface from the surface to ~ 15 –20 km depth.

[13] Figure 5 shows the cross correlations filtered at 3–10 s periods between a broadband station CLC and other distant stations from the SCSN as well as between a short-period station WRC and other SCSN stations. The locations of the stations CLC and WRC situated near the Coso geothermal area are shown in Figure 1a. Surface wave signals appear at either positive or negative correlation lag times with an average moveout speed of ~ 3 km/s, as delineated by the inclined dashed lines. The waveforms of cross correlations between short-period stations or broadband stations are very similar between 3 and 10 s periods. To simplify data analysis and enhance the SNR, we separate each cross correlation into positive and negative lag components and then add the two components to form a final cross correlation, called the “symmetric component.” The following analyses are performed exclusively on symmetric components.

4. Dispersion Measurements and Data Selection

[14] *Bensen et al.* [2007] showed that uncertainties of group velocity dispersion measurements from cross correlations are much larger than those of phase velocity measurements. Thus, we only construct phase velocity dispersion maps between 3 and 10 s periods and then use these maps to invert for a 3-D shear wave velocity model of the subsurface. Phase velocity dispersion measurements of Rayleigh waves are obtained from the symmetric components of interstation cross correlations by automatic frequency–time analysis (FTAN) [e.g., *Bensen et al.*, 2007].

[15] Figure 6 shows two examples of measured phase velocity dispersion curves. The path between stations CGO and LRL (red line) passes through the Coso geothermal area, while the path between stations CWC and TEH (blue line) passes through the Sierra Nevada. Phase velocities of the CGO–LRL path (red line) are significantly lower than those of the CWC–TEH path, which indicates generally lower seismic velocities in the Coso geothermal area and higher velocities in the Sierra Nevada.

[16] The automated FTAN dispersion measurements are winnowed by applying three criteria to select reliable measurements for surface wave tomography. First, the distance between two stations must

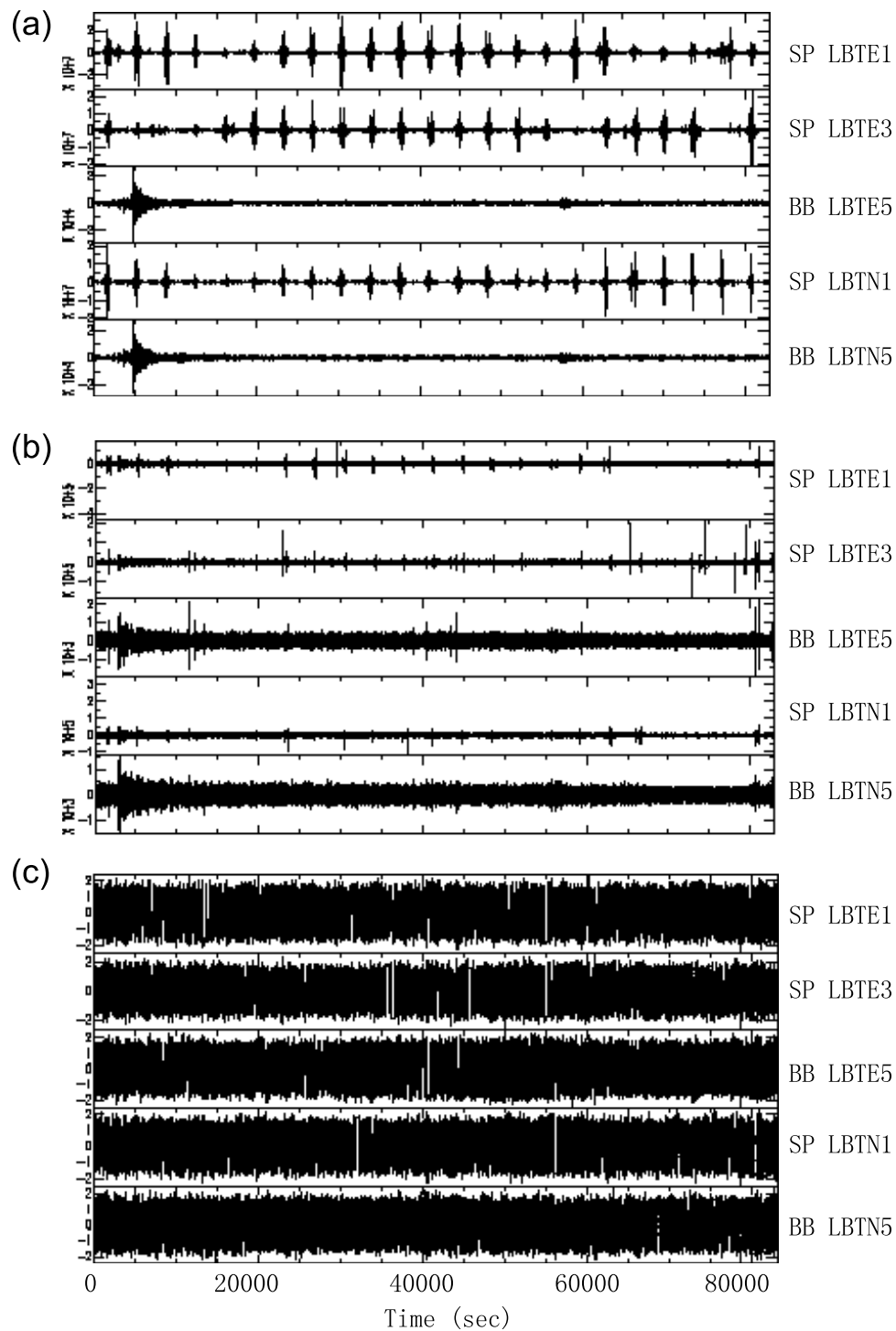


Figure 3. (a) Examples of daily time series for five stations from the Coso PASSCAL experiment. Time series for short-period stations LBTE1, LBTE3, and LBTN1 display a series of glitches, whereas broadband stations LBTE5 and LBTN5 do not. (b) Band-pass filtering time series from 0.1 to 1 Hz (1–10 s period) reduces glitches compared to those in Figure 3a. (c) Applying running-absolute-mean normalization to the time series shown in Figure 3b suppresses glitches further.

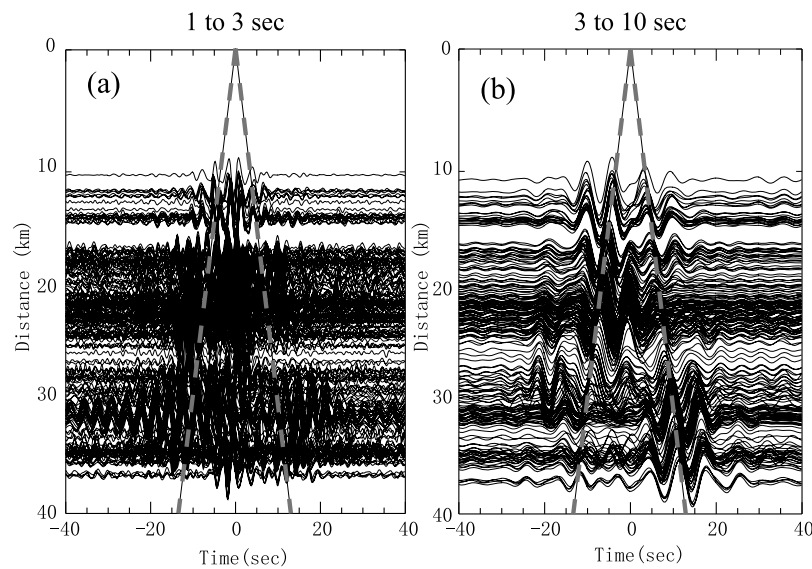


Figure 4. One month cross correlations from June 1999 among the Coso PASSCAL stations from periods of (a) 1 to 3 s and (b) 3 to 10 s, respectively. The inclined dashed lines indicate the 3.0 km/s moveout. Clear surface wave signals appear in the cross correlations from 3 to 10 s periods (Figure 4b) but not from 1 to 3 s.

be greater than three wavelengths to ensure that full surface wave packets can be separated from precursory noise and interpreted as far-field measurements [Tsai and Moschetti, 2010]. Second, the signal-to-noise ratio (SNR) must be higher than 15 at an individual period for the measurement at that period to be accepted. SNR is defined as the ratio of the peak amplitude within a time window containing the surface wave signal to the root-mean-square of the noise trailing the signal arrival window. Third, we require that the measurements agree with one another across the data set. This condition is tested during tomography as discussed in section 5. Measurements that can be fit well by a smoothed tomographic map are considered to cohere with the data set as a whole.

[17] Our data selection criteria result in a maximum of 590 measurements at 6 s periods being chosen for tomography from the ~6000 original interstation velocity measurements. The numbers of selected paths as a function of period are listed in Table 1. The final number declines at smaller periods, so that there are only about 310 measurements chosen for tomography at 3 s periods because ambient noise at periods shorter than 5 s is very weak. The number also reduces above 6 s periods, mainly due because of the three-wavelength criterion for interstation distances.

[18] We compute uncertainties for the dispersion measurements based on repeating cross correlations over different time spans, as Yang *et al.* [2007] did

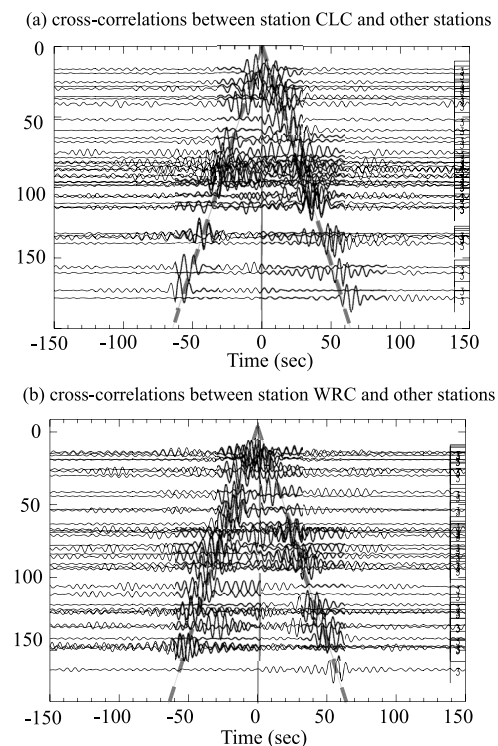


Figure 5. One month cross correlations for June 2008 filtered between periods of 3 and 10 s for (a) broadband station CLC and other stations and (b) short-period station WRC and other stations. Clear Rayleigh waves at 3–10 s periods appear for both broadband and short-period stations with a propagation of about 3 km/s, as delineated by the two inclined dashed lines. Locations of stations CLC and WRC are indicated in Figure 1.

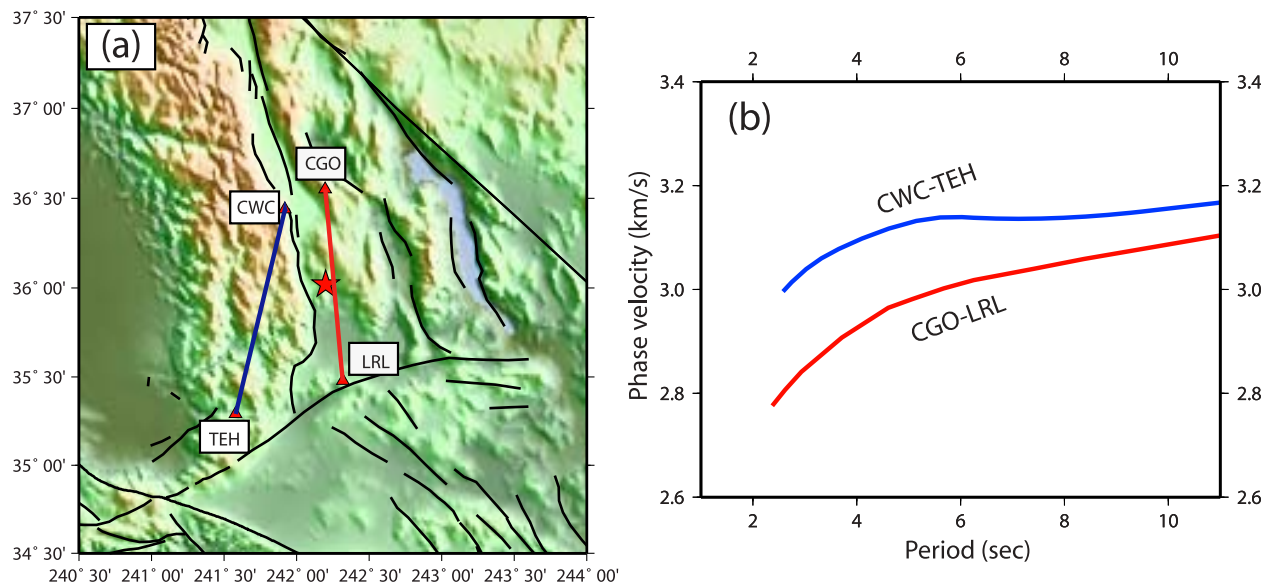


Figure 6. (a) Raypaths between stations CGO and LRL (red) and between stations CWC and TEH (blue). The red star marks the location of the Coso geothermal area. (b) The measured Rayleigh wave phase speed dispersion curves are based on the symmetric components; the red curve is for station pair CGO-LRL and the blue curve for CWC-TEH. Phase velocities of the path CGO-LRL path (red lines) through the Coso geothermal area are depressed compared with the path between stations CWC-TEH that transits the Sierra Nevada Mountains.

using individual 3 month cross correlations. Because the installation durations of individual subarrays of the Coso PASSCAL experiment vary from 1 to 3 months, time series lengths of stacked cross correlations range from 1 to 3 months. Given the short time lengths of cross correlations, it is inappropriate to perform uncertainty analysis of measurements from the Coso PASSCAL stations. Thus, we only estimate measurement uncertainties for cross correlations between SCSN stations. The average uncertainties of phase velocity measurements between the SCSN stations are about 20 m/s to 30 m/s with slightly higher uncertainties at longer periods, about 0.7–1.0% of the measured phase velocity values.

5. Surface Wave Tomography and Construction of a 3-D Shear Velocity Model

[19] We perform surface wave tomography on the selected dispersion measurements to produce Rayleigh wave phase velocity maps on a 0.25° by 0.25° grid using the method of *Barmin et al.* [2001]. This tomography is performed in two steps. In the first, preliminary, step, an overly smoothed map is generated at each period in order to identify and reject bad measurements. This composes the third selection criterion discussed in section 4. We discard

phase velocity measurements with travel time residuals larger than 2 s. The second step of tomography is the construction of the final phase velocity maps that are laterally smoothed less than the maps constructed in the first step. The tomography method also provides corresponding resolution information. Examples of resolution maps and associated path coverage at 4 and 9 s periods are plotted in Figure 7. Resolution is estimated to be about 40 km in most areas of the study region, but degrades toward the fringes.

[20] The resulting phase velocity maps at 3, 5, 7 and 9 s periods are shown in Figure 8. Velocity perturbations are only plotted in the areas encompassing stations as outlined by the pentagons. The

Table 1. The Numbers of Selected Paths for Tomography at Different Periods

Period (s)	Number of Paths
3.00	310
3.50	362
4.00	454
4.50	490
5.00	491
6.00	590
7.00	571
8.00	459
9.00	365
10.00	288

most pronounced features are high Rayleigh wave velocities along the Sierra Nevada and low velocities in the basin and range province to the east of the Sierra Nevada, especially near the Coso geothermal area. We do not discuss the observed variations of the phase velocity maps in detail because they are inverted for a 3-D V_s model, which we discuss later in the paper.

[21] Example local dispersion curves for a point in the Sierra Nevada and at the Coso geothermal area (Figure 9a) extracted from the phase velocity maps from 3 to 10 s periods are shown in Figure 9b. These and similar curves elsewhere are inverted for V_s profiles beneath all grid points. Vertical V_s profiles beneath these two locations are shown in Figure 9c. The model is strongly damped vertically to ensure that vertical differences between nearby layers are minimal. The 3-D V_s model then is constructed by assembling all of the V_s profiles. To demonstrate the resolution capability of Rayleigh wave dispersion measurements between 3 and 10 s periods to constrain shear velocities at various depths, sensitivity kernels of Rayleigh wave phase velocities to shear velocities at the Coso geothermal field are plotted in Figure 10. The shortest period Rayleigh wave of 3 s in this study has fair sensitivity to the top 2 km and the longest period of 10 s has peak sensitivity at around 10 km depth and fair sensitivity up to ~20 km. Thus, using the dispersion curves from 3 to 10 s periods allows us to constrain shear velocities from the surface to ~20 km depth.

[22] To construct the V_s model we perform a linearized inversion of each Rayleigh wave phase speed curve for the best fitting V_s model below each grid point. In the linearized inversion, depth-dependent shear wave speeds are parameterized in eight layers from the surface to a depth of 20 km with the thickness varying from 2 km at the surface to 5 km at 20 km depth. Partial derivatives of phase velocity at each period relative to V_s at various depths are calculated using the method of Saito DISPER80 [Saito, 1988]. During the inversion, adjacent layers of the V_s model are smoothed vertically between neighboring layers in order to reduce the likelihood of vertical oscillations in the model. At most places a vertically smooth model can fit the data quite well, but in section 6 we discuss further the effect of weakening this constraint in the Coso geothermal area. Because Rayleigh wave phase speeds depend primarily on V_s , we scale V_p to V_s using a constant V_p/V_s ratio of ~1.73, which approximately is the average V_p/V_s ratio found by *Hauksson and Unruh* [2007]. We take the one-dimensional aver-

age model of *Hauksson* [2000] as the starting model in our model.

[23] Although we estimated uncertainties in most of the dispersion measurements, we do not have estimates of uncertainties in the shear wave velocity structure. However, misfit to the measurements from the 3-D model is approximately constant with period and averages between 40 m/s and 50 m/s, which is a fairly good estimate of the uncertainty in the local dispersion curves, such as those shown in Figure 9b.

6. Discussion

[24] Figure 11 shows the maps of shear velocity at depths of 1, 3, 6, 10, 14, and 18 km plotted as perturbations relative to the average values across the maps at each depth. The most pronounced high velocity is observed beneath the Sierra Nevada, which is composed primarily of Mesozoic granitic plutons and is probably colder and less faulted than other regions in this study area [e.g., *Saltus and Lachenbruch*, 1991; *Combs*, 1980]. The eastern margin of this high-velocity anomaly follows the eastern front of the Sierra Nevada in the top 6 km but gradually retreats toward the west at greater depths. This westward retreat with depth suggests that Sierran crust is being modified from below, either thermally [e.g., *Saltus and Lachenbruch*, 1991] or mechanically by west dipping low-angle normal faults [e.g., *Wernicke*, 1985; *Jones*, 1987; *Jones and Phinney*, 1998]. Within the southern Sierra Nevada, low velocities are imaged in the top 3 km of the crust near Lake Isabella, which may be due to the presence of sediments or deformation associated with the proto-Kern Canyon or Kern Canyon fault zones. In the upper crust (<10 km), prominent low velocities are imaged beneath the Coso geothermal area, which are probably related to high temperatures and perhaps the presence of partial melt. The depth range of these low velocities is consistent with receiver function studies, such as *Wilson et al.* [2003]. This is discussed further below. Another pronounced shallow low velocity is also imaged near 242° 15' just south of the Garlock Fault. Velocities in the uppermost 2 km and 6–10 km beneath northern Death Valley are also low. In the middle crust from 10 to 20 km, the most pronounced feature is the low velocities beneath the southern Great Valley, perhaps reflecting deeper sediments than expected, Miocene tectonism, or possibly Rand schist in the lower crust [e.g., *Bartow*, 1984].

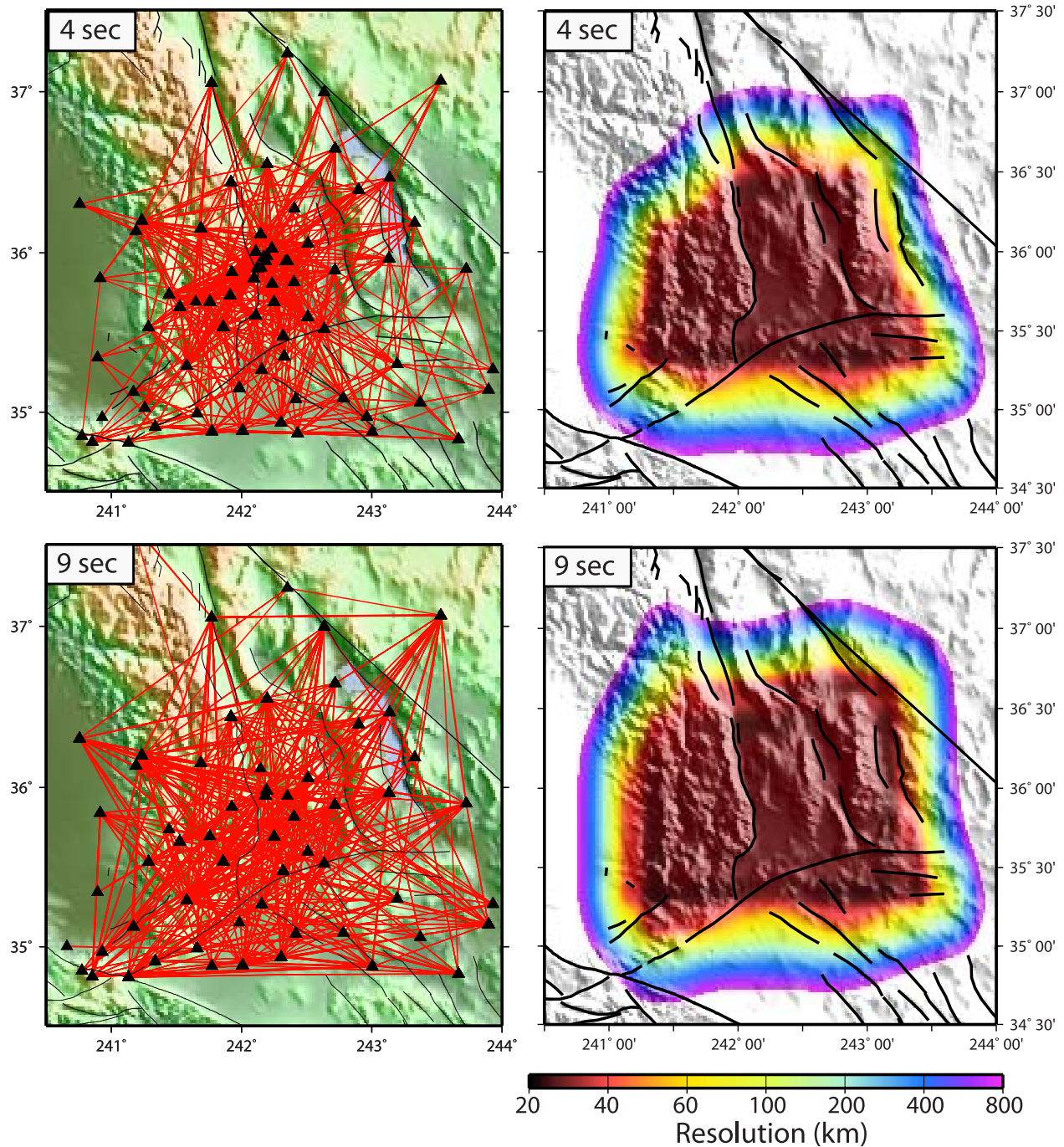


Figure 7. Path coverage and resolution at periods of 4 and 9 s for Rayleigh wave phase speed tomography on a $0.25^\circ \times 0.25^\circ$ grid.

[25] In general, the 3-D model of shear velocity structure (Figure 11) displays anomalies that correlate with surficial geologic features, suggesting that the analysis has captured wave speed variations reflecting local geology. Most prominent are the high velocities beneath the Sierra Nevada, consistent with the relatively unfaulted plutonic

framework of the range. Bedrock in the mountains north of the Garlock Fault also tend to have higher waves speeds than average in the top 5 km of the crust with the notable exception of the Coso Range and, perhaps, the southern Inyo Mountains. Sedimentary basins are less distinctly imaged. The Cantil Basin just south of the Garlock Fault near

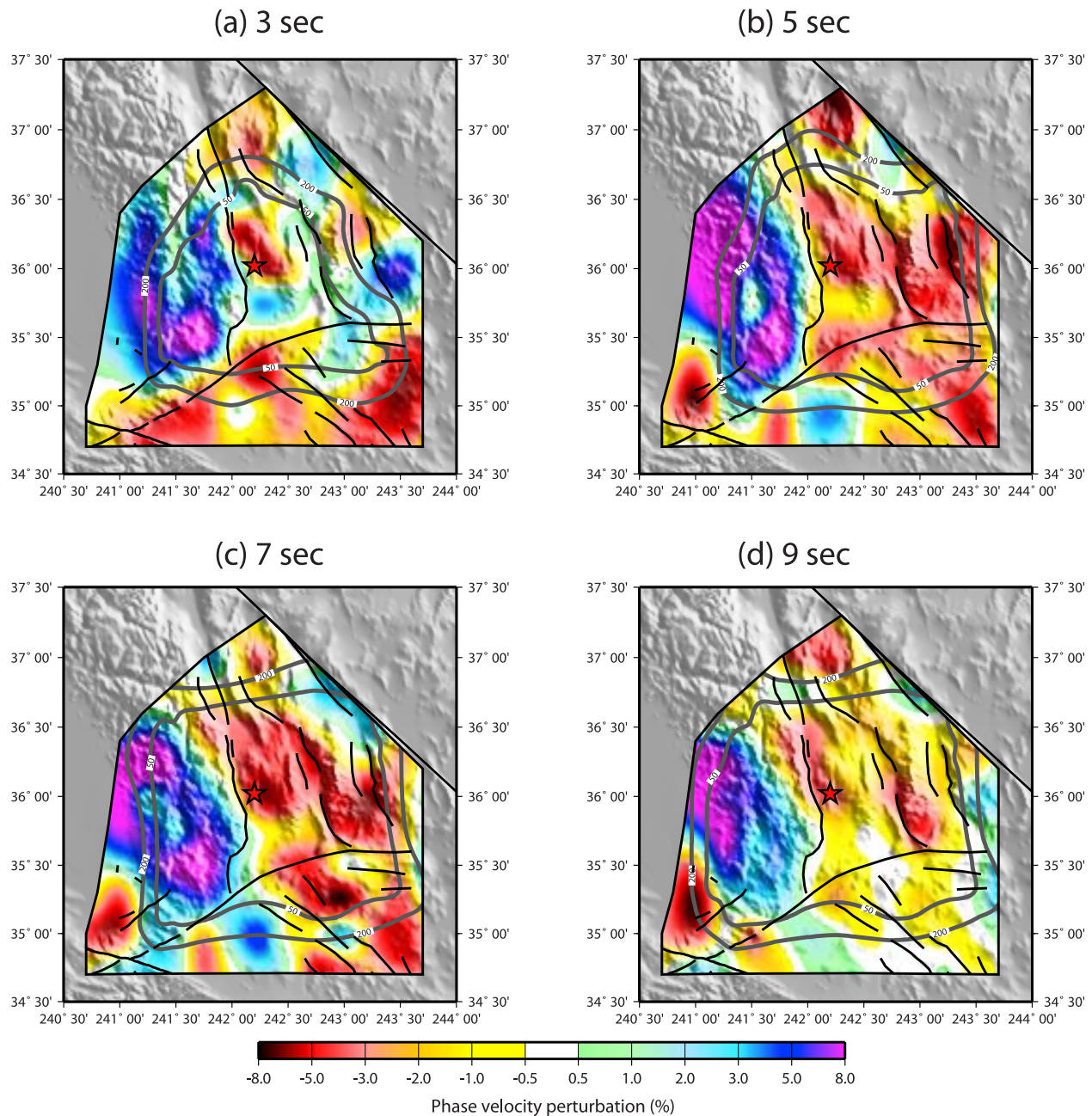


Figure 8. Phase velocity maps at periods of 3, 5, 7, and 9 s. Velocity perturbations relative to the averages across each map are plotted in the region encompassing the stations, as outlined by the polygons. Two gray contours indicating resolution of 50 and 200 km are plotted on each phase velocity map.

longitude 242.25° is a notable low velocity feature at ~ 1 km depth, consistent with both the substantial gravity low in the basin and seismic reflection imaging [e.g., Pullammanappallil and Louie, 1993]. Death Valley is also a prominent shallow low, consistent with the accumulation of sediments in that basin [e.g., Blakely et al., 1999]. Other prominent basins, such as Owens Lake and Indian Wells Valley, are not particularly evident in the inversion

results. The absence of Indian Wells Valley in particular, given its presence in P wave images of *Hauksson and Unruh [2007]*, suggests either an error in one analysis or the other or the presence of unusual valley fill with a very low V_p/V_s ratio.

[26] An intriguing feature that emerges in this study is the low velocities between about 6 and 8 km depth under much, but not all, of the basin and

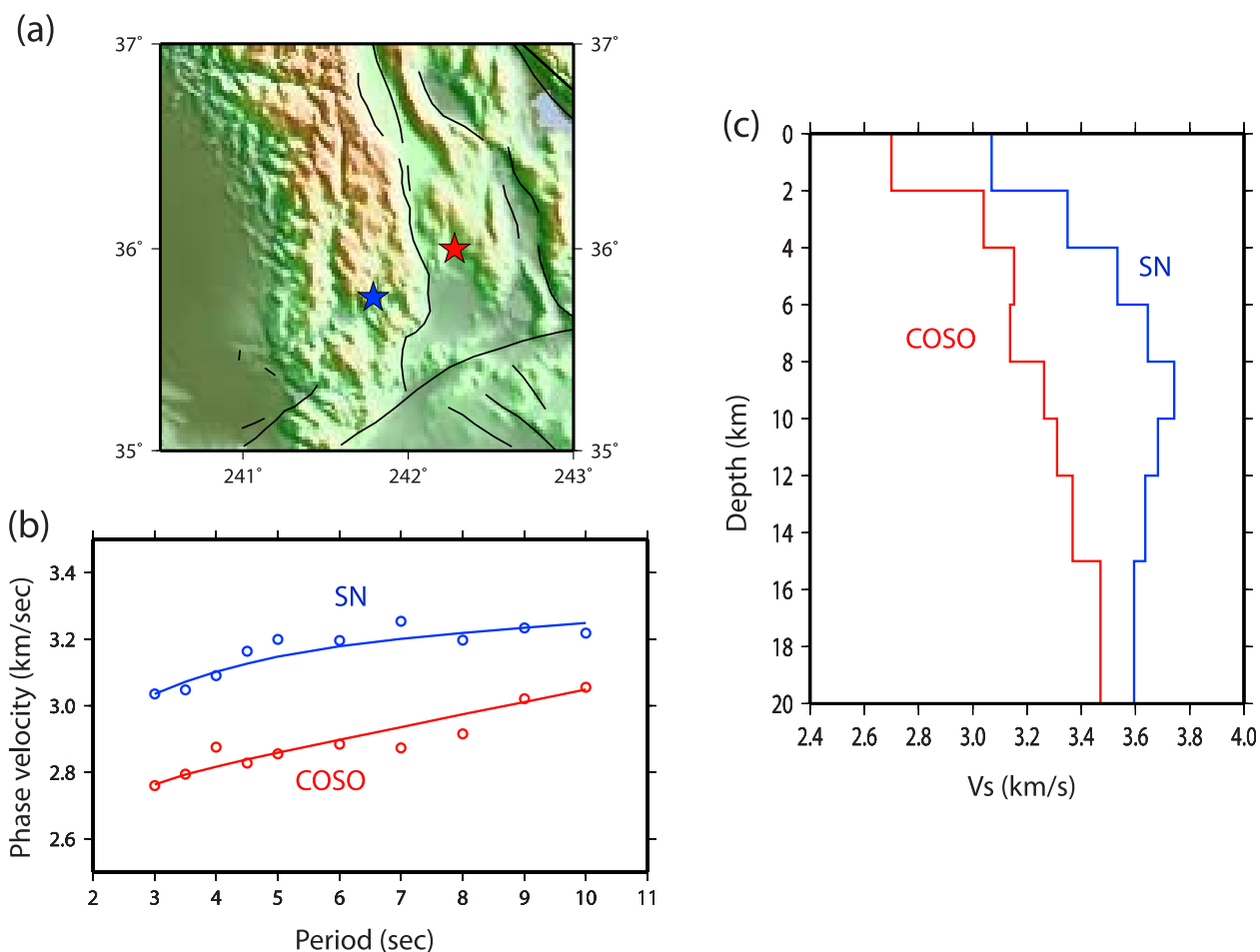


Figure 9. (a) Location of two points in the Sierra Nevada (blue star) and near the Coso geothermal area (red star) to illustrate inversion results. (b) Rayleigh wave phase velocity dispersion curves from the dispersion maps (circles) for the two locations shown in Figure 9a. The solid lines are the dispersion curves produced by (c) the V_s model estimated by linearized inversion, shown. Red lines and symbols are for the Coso point, and blue lines and symbols are for the Sierra Nevada.

range (Figures 11c and 12). This feature correlates well with the extent of sizable exposures of Neogene and Quaternary volcanic rocks (Figure 12), strongly suggesting a magmatic origin. Within the area well resolved by this study, only the older Miocene volcanic center in the southern Sierra and some small volume centers in the eastern Sierra remain outside this zone. It is implausible that this entire feature represents uniformly distributed melt at these depths, but local accumulations of melt seem consistent with very low resistivities found near these depths north of Coso [Park and Wernicke, 2003]. This anomaly probably results from crust profoundly reworked by igneous processes over the past few million years. The modern low velocities may represent some combination of melt, alteration, magmatic fluids and high temperatures. We explore some aspects of this feature more thoroughly in the vicinity of the Coso Volcanic Field, where this

feature is better sampled and where other work, summarized in section 1, provides some constraints on the nature of this anomaly.

[27] Three vertical V_s transects are plotted as absolute and relative velocities in Figure 13, with the positions of these V_s transects indicated on the 1 km shear velocity map (Figure 11a). Low velocities in the entire depth column beneath the Coso Range are quite close to the position of the Coso geothermal field. In particular, there is a very low velocity feature imaged in the top 2 km. The appearance of this anomaly, despite the dominant surface exposure of granite, suggests profound alteration of the crust in the area and/or significant influence from shallow magmatic or hydrothermal fluids. This feature, absent at equivalent depths from the local earthquake tomography of Hauksson and Unruh [2007], appears to underlie the northern part of

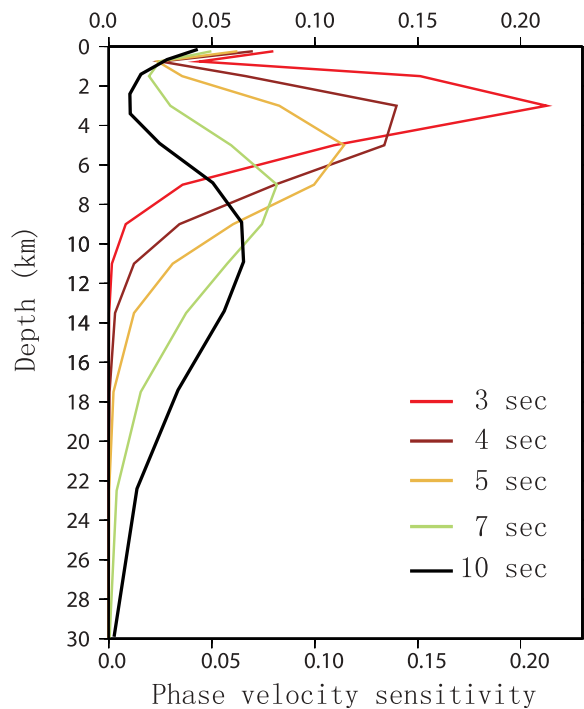


Figure 10. Sensitivity kernels of Rayleigh wave phase velocities to shear velocities at periods of 3, 4, 5, 7, and 10 s at the Coso geothermal field (red star shown in Figure 9).

the rhyolite domes of the Coso Volcanic Field and extend under the northern Coso Range. The area immediately south and east of the geothermal field has relatively high velocities.

[28] Although the entire crustal column beneath the Coso geothermal area appears to have depressed V_s speeds (Figures 9c and 13), there is an indication of a low-velocity zone between depths of 6 and 8 km. This may reflect a deeper magmatic anomaly underlying the shallow geothermally induced anomaly in the top 2 km. The absence of profound low velocities below ~ 14 km (Figure 11e) tends to support a shallow magmatic interpretation. As noted above, these low velocities between 6 and 8 km depth extend over much of the region (e.g., beneath Death Valley, Figure 13, A-A'), although several studies discussed low-velocity zones beneath Death Valley [e.g., *de Voogd et al.*, 1986] and suggested a magmatic origin. Thus, it is important to test the resolvability of a shallow magmatic body (6–10 km) and the ability to separate such a body from anomalies above and below it.

[29] As a first test to gain insight into vertical resolution, we consider dispersion curves for low-velocity anomalies in depth ranges from 1 to 4 km (red), 6 to 10 km (pink), and 10 to 15 km (blue),

respectively, as seen in Figure 14a. The amplitude of the velocity anomaly is 10% for the whole low-velocity body. Rayleigh wave phase velocities from these models are presented in Figure 14b together with a background model. Inspection of the dispersion curves shows that to resolve anomalies at depths from 1 to 4 km from those at 6 to 10 km requires observations below 6 s periods, which we have. Resolving shallow and deep magmatic bodies at 6–10 km versus 10–15 km is harder, however. Measurements below 6 s periods are still needed, but the phase speed differences presented by these anomalies are smaller. In this case, with a 10% anomaly, differences are only about 50 m/s, which is approximately equal to the uncertainty in the phase speed maps.

[30] Second, to test the vertical and lateral resolution we consider the ability to image three depth anomalies similar to those in the previous test, but with depth ranges that differ slightly from those in Figure 14. The initial model is laterally homogeneous and taken from the average of the inversion with real data except a low-velocity anomaly is introduced beneath the Coso geothermal area. The lateral extent of this low-velocity body is a $0.5^\circ \times 0.5^\circ$ square centered at 117.875° , 36.125°N . We plot cross sections of the input V_s structures in Figure 15 (left column) along latitude 36.125°N . From the three input models under each grid node, we first calculate the dispersion curves from 3 to 10 s periods for Rayleigh wave phase velocities. Then, we construct phase velocity maps at the individual periods. At each period, we calculate the travel times and the average phase velocities between individual paths as in our real data. We also add Gaussian random noise with a 0.5 s standard deviation to the travel times of individual paths, similar to the standard deviation of the misfit in the tomography with real data. Using the calculated phase velocities of paths at different periods as the synthetic data, we perform the same inversion as described for the real data; that is, constructing phase velocity tomography maps, then extracting phase velocity dispersion curves at each grid from phase velocity maps, and finally inverting for shear wave velocities beneath each grid to construct a 3-D V_s model. Cross sections of the recovered V_s structure are plotted in Figure 15 (right column) for comparison with the input. The shape of a low-velocity body between 0 and 6 km depth is recovered quite well, with limited vertical smearing. However, the deeper anomalies are smeared significantly vertically. The anomaly between 4 and 10 km is smeared at both top and bottom, but only at

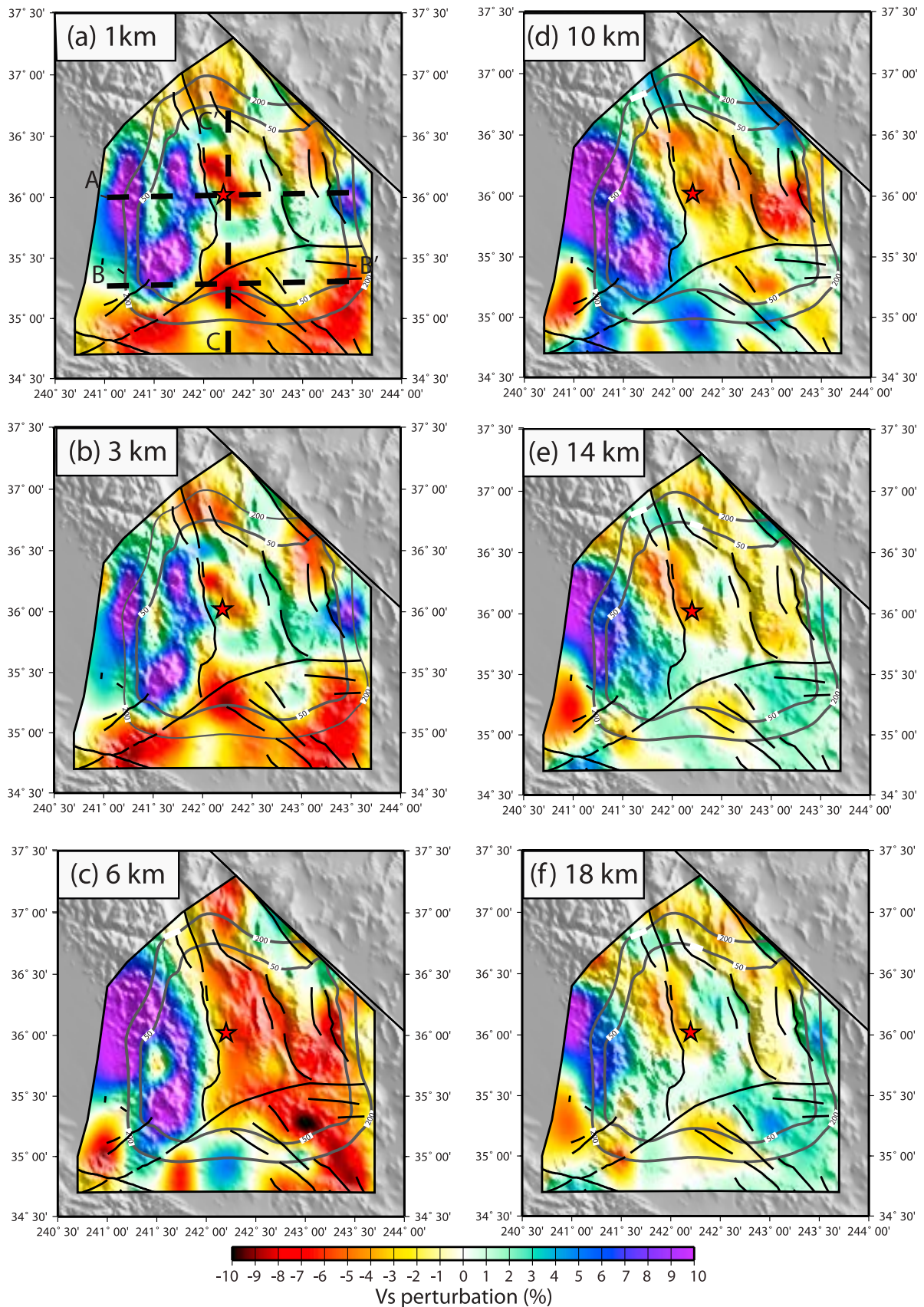


Figure 11

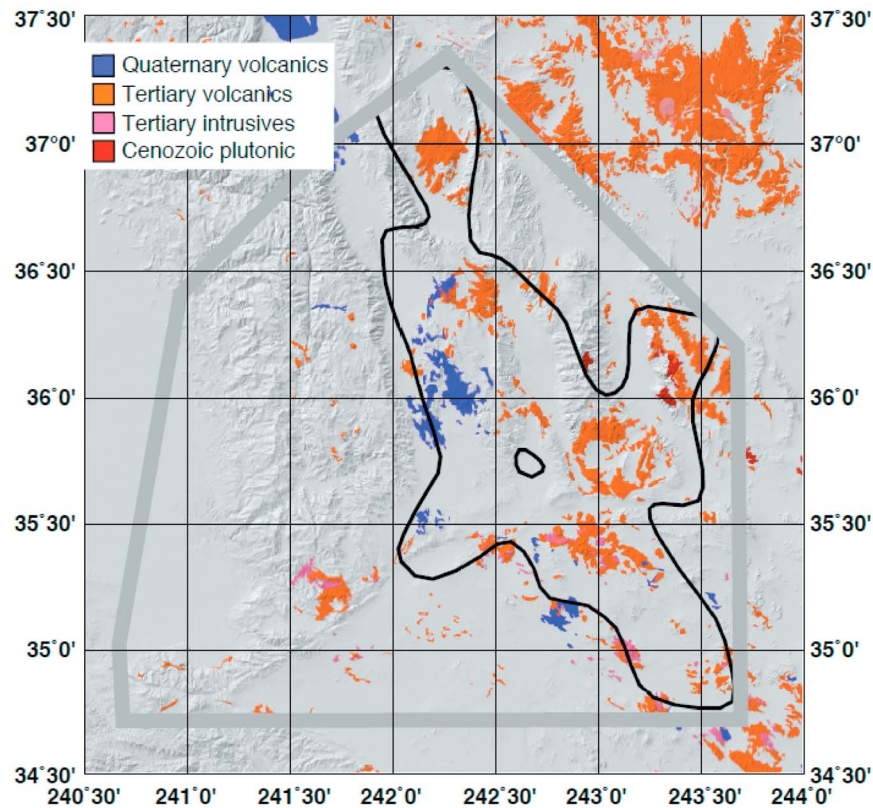


Figure 12. Exposures of Cenozoic igneous rocks in eastern California [Jennings, 1977; Crafford, 2007] compared with outline (black) of low V_s ($< \sim 3\%$ at 6 km depth, Figure 11c). Extent of inverted region delineated by gray outline.

the bottom for the anomaly at 8–16 km. For all cases, the amplitude of the anomaly is damped by $\sim 50\%$. The extent of amplitude damping would increase for thinner bodies.

[31] As a final test, we reconsider the inversion of the dispersion data near the Coso geothermal area, shown in Figure 9b. In Figure 16, however, we reduce the strong vertical smoothing applied in the inversion across the entire area. We see that reducing smoothing results in amplifying the low-velocity zone between depths of 8 and 12 km while increasing the velocities at 15 km and below. Thus, although the strength of the low-velocity zone between 6 and 12 km is not well constrained, a confined low-velocity zone beneath 14 km is inconsistent with our data.

[32] In conclusion, the resolution tests show that our data and methods are able to resolve a low-velocity body situated in the top 5 km. Deeper anomalies are harder to resolve, but the absence of prominent low velocities beneath about 14 km depth in our estimated model (Figures 11 and 13) beneath the Coso geothermal area is inconsistent with a deep seated magmatic source below this depth. The somewhat depressed low velocities observed between 6 and 8 km (Figure 13, A-A') may reflect a magmatic body near this depth whose velocity anomaly is underestimated due to the intrinsic limitations in resolution in this depth range and the fact that we have strongly smoothed the model in the inversion. Applying somewhat less vertical smoothing further reduces V_s speeds between 8 and 12 km beneath the Coso geothermal

Figure 11. Maps of Rayleigh wave shear velocity at depths of 1, 3, 6, 10, 14, and 18 km are plotted as perturbations to averages at each depth: (a) 1 km (2.867 km/s), (b) 3 km (3.174 km/s), (c) 6 km (3.319 km/s), (d) 10 km (3.452 km/s), (e) 14 km (3.524 km/s), and (f) 18 km (3.574 km/s). Two gray contours of resolution at resolution scales of 50 and 200 km from the 5 s phase velocity map (Figure 8b) are plotted in each map. The three dashed lines in Figure 11a delineate the surface locations of the three vertical transects shown in Figure 13.

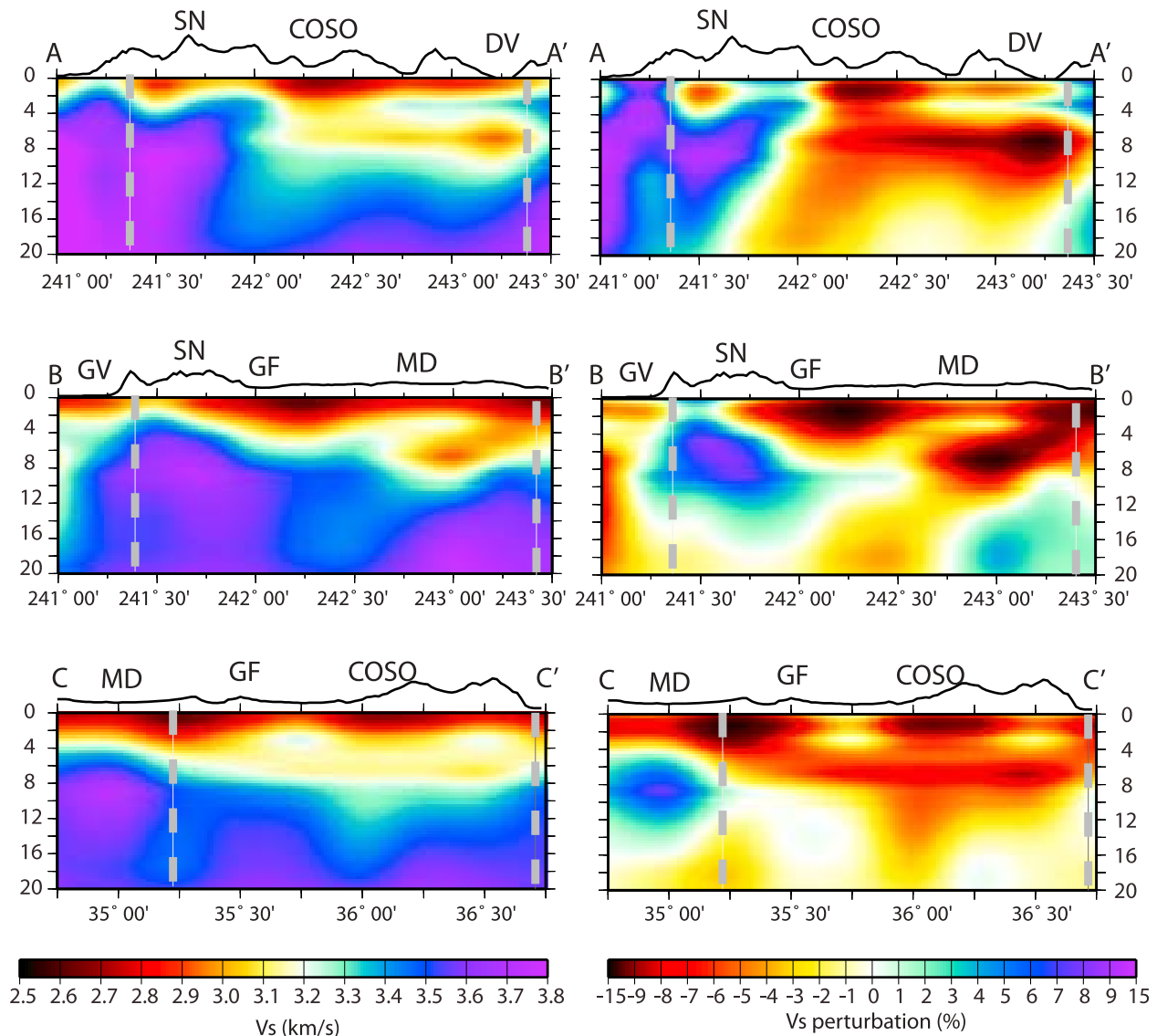


Figure 13. Vertical cross sections of shear velocities plotted as both (left) absolute values and (right) perturbations relative to the 1-D V_s averages. The two dashed gray lines in each plot indicate that the area between these two lines has a lateral resolution of 50 km, corresponding to the 50 km resolution contour in Figure 11a. The locations of the cross sections are shown in Figure 11a. Abbreviations: COSO, the Coso geothermal area; SN, the Sierra Nevada Mountains; DV, Death Valley; MD, Mojave Desert; GV, California's Great Valley; GF, Garlock Fault.

area, as seen in Figure 16. This is consistent with the existence of a magmatic body within the depth range from 6 to 12 km beneath the Coso geothermal area. The causative body may be much thinner than this. It must be noted, however, that this interpretation is pushing the resolution limits of this study.

7. Summary and Conclusions

[33] We processed continuous seismic data from a PASSCAL experiment that operated between 1998

and 2000 as well as surrounding broadband stations from the Southern California Seismic Network (SCSN). Daily cross correlations were performed between all pairs of stations that overlapped in time of deployment and were then stacked over the deployed durations. SNR and phase and group velocities of Rayleigh waves were measured with an automated FTAN procedure for each stacked cross correlation. Then, three selection criteria determined the reliable measurements for surface wave tomography, which numbered between 288 and 590 paths across the study region, depending on period.

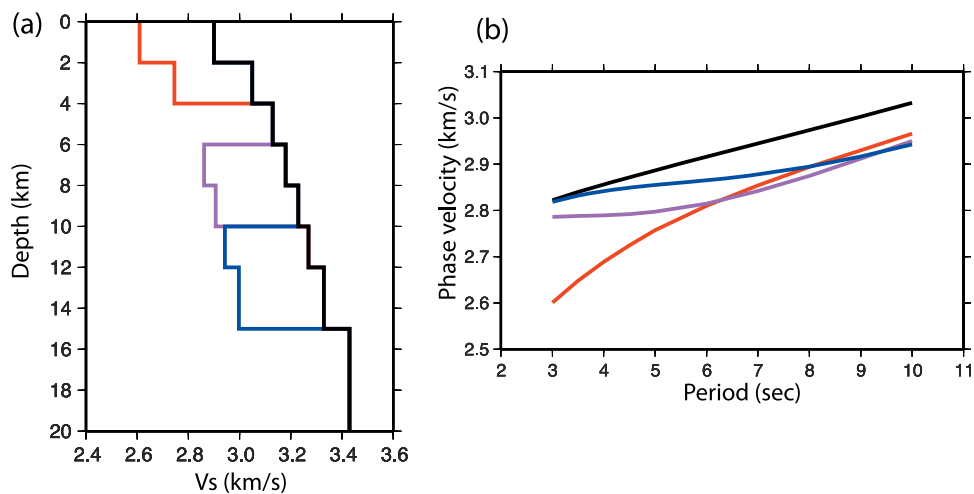


Figure 14. Comparison of Rayleigh wave phase velocity curves from four different vertical profiles: background model containing no low-velocity zones (black), 10% low-velocity anomaly in the top 4 km (red), 10% low-velocity anomaly between depths of 6 and 10 km depth (pink), and 10% low-velocity anomaly between 10 and 15 km depth (blue). (a) Plots of the velocity profiles for the four models. (b) The associated dispersion curves.

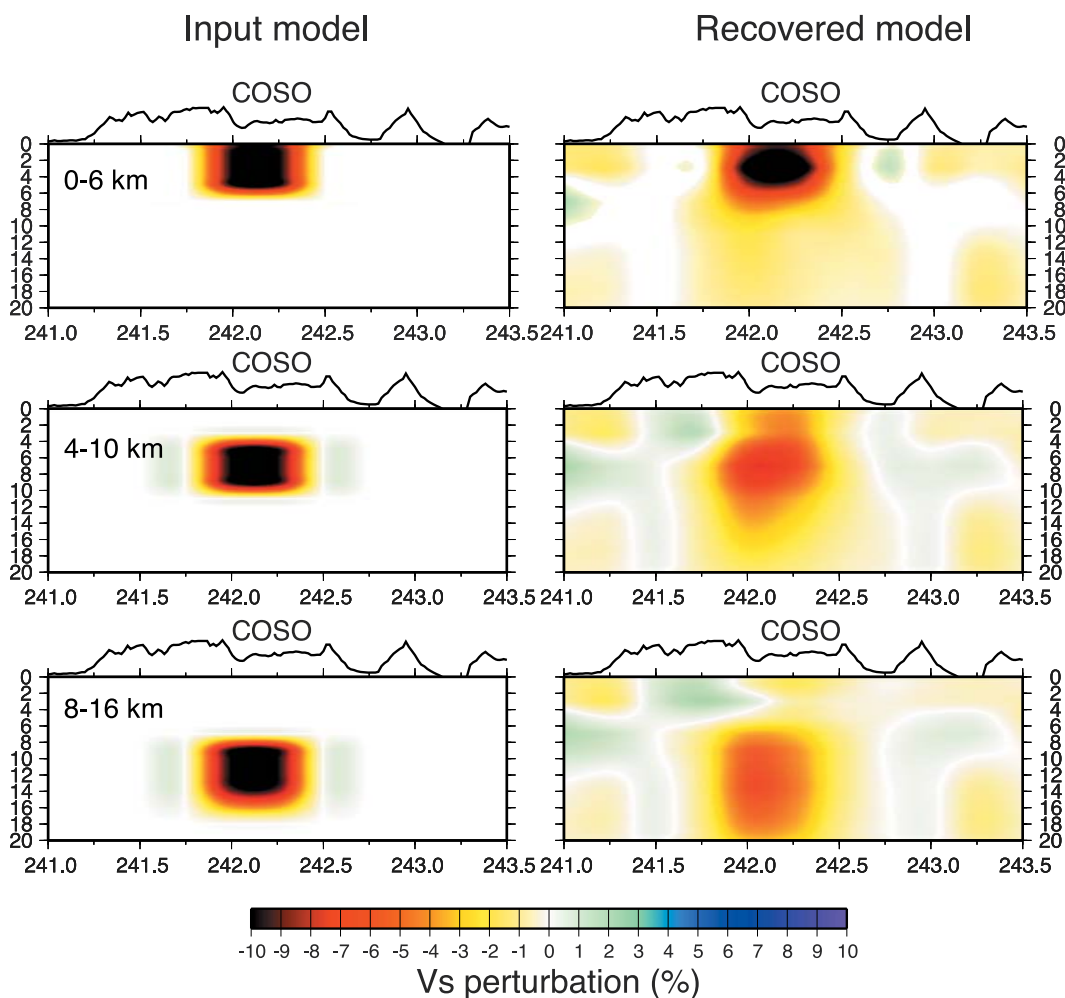


Figure 15. Resolution tests for three input V_s models with low-velocity anomalies at different depths. (left) Input models with low-velocity bodies at 0–6 km, 4–10 km, and 8–16 km depth. (right) The recovered models.

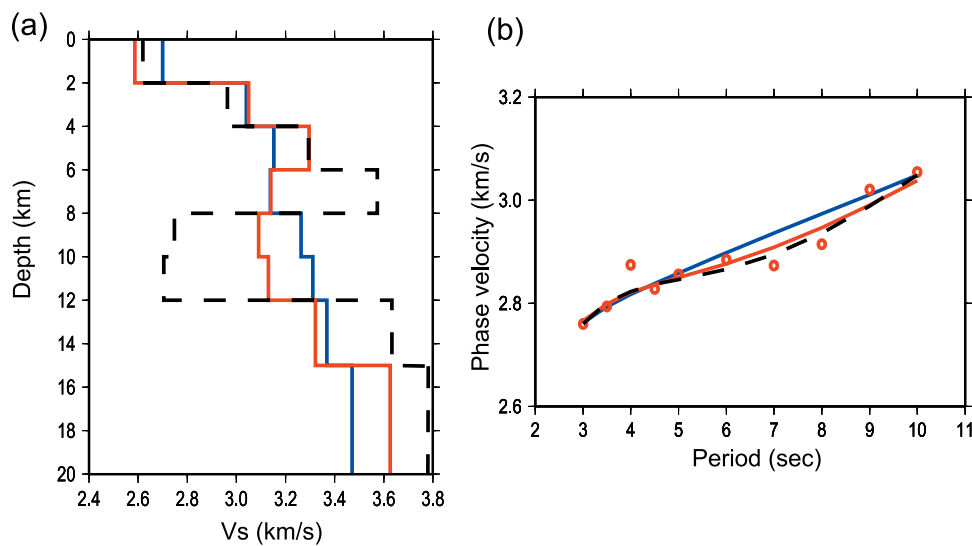


Figure 16. Effect of changing vertical smoothing on inversions for the V_s structure directly beneath the Coso geothermal area. (a) Resulting models from three different vertical smoothing schemes; blue indicates strongly smoothed as in our inversions shown in Figures 11, 13, and 15 (same as Figure 9c), red indicates less strongly smoothed, and black dashed lines indicate even less vertical smoothing. (b) The dispersion data from 3 to 10 s periods near the Coso geothermal area (red circles, same as Figure 9b) and the resulting dispersion curves from each differently smoothed inversion, similarly colored. Strong vertical smoothing reveals a very weak low-velocity zone from 6 to 8 km depth. Reducing smoothing produces a stronger low-velocity anomaly between depths of 6 and 12 km and increasingly higher velocities below 15 km depth.

[34] We inverted all of the phase velocity measurements for phase velocity maps between periods of 3 and 10 s and the resulting phase velocity maps for a 3-D shear velocity model by a strongly vertically smoothed linearized inversion. This 3-D model reveals generally depressed shear velocities beneath the Coso geothermal area and also a prominent low shear velocity anomaly within the top 2 km, no significant anomaly below about 14 km depth, and a weakly resolved low-velocity anomaly between 6 and 12 km depth. The anomaly in the top 2 km is believed to result from geothermal alteration in the shallow subsurface. No magmatic body is imaged beneath 14 km depth, but the shear velocity anomaly between 6 and 12 km may be due to partial melt associated with a magma body. The amplitude of the inferred V_s anomaly for this body is dependent on its vertical thickness and the extent of vertical damping in the inversion. For this reason, the amplitude of this anomaly is ill determined. This anomaly may be representative of magmatic processes that have altered the crustal structure through much of eastern California.

Acknowledgments

[35] The authors thank Wei-Chuang Huang for valuable conversations. Data used in this study result from a PASSCAL

experiment performed from November 1998 to May 2000 and from the Southern California Seismic Network. Facilities of the IRIS Data Management System, and specifically the IRIS Data Management Center, were used to access the waveform and metadata required in this study. The IRIS DMS is funded by the National Science Foundation and specifically the GEO Directorate through the Instrumentation and Facilities Program of the National Science Foundation under Cooperative Agreement EAR-0552316. This study was supported by the Navy Geothermal Program Office (GPO) under contract N68936-08-C-0061. This is contribution 702 from the Australian Research Council National Key Centre for the Geochemical Evolution and Metallogeny of Continents (<http://www.gemoc.mq.edu.au>).

References

- Armstrong, R. L., and P. Ward (1991), Evolving geographic patterns of Cenozoic magmatism in the North American Cordillera: The temporal and spatial association of magmatism and metamorphic core complexes, *J. Geophys. Res.*, *96*, 13,201–13,224, doi:10.1029/91JB00412.
- Barmin, M. P., M. H. Ritzwoller, and A. L. Levshin (2001), A fast and reliable method for surface wave tomography, *Pure Appl. Geophys.*, *158*, 1351–1375, doi:10.1007/PL00001225.
- Bartow, J. A. (1984), Geologic map and cross sections of the southeastern margin of the San Joaquin Valley, California, *U.S. Geol. Surv. Misc. Invest. Map, I-1496*, 2 sheets, scale 1:125,000.
- Bensen, G. D., M. H. Ritzwoller, M. P. Barmin, A. L. Levshin, F. Lin, M. P. Moschetti, N. M. Shapiro, and Y. Yang (2007), Processing seismic ambient noise data to obtain reliable

- broad-band surface wave dispersion measurements, *Geophys. J. Int.*, *169*, 1239–1260, doi:10.1111/j.1365-246X.2007.03374.x.
- Bensen, G. D., M. H. Ritzwoller, and N. M. Shapiro (2008), Broadband ambient noise surface wave tomography across the United States, *J. Geophys. Res.*, *113*, B05306, doi:10.1029/2007JB005248.
- Bensen, G. D., M. H. Ritzwoller, and Y. Yang (2009), A 3-D shear velocity model of the crust and uppermost mantle beneath the United States from ambient seismic noise, *Geophys. J. Int.*, *177*, 1177–1196, doi:10.1111/j.1365-246X.2009.04125.x.
- Bhattacharyya, J., and J. M. Lees (2002), Seismicity and seismic stress in the Coso Range, Coso geothermal field, and Indian Wells Valley region, southeast-central California, *Mem. Geol. Soc. Am.*, *195*, 243–257.
- Bhattacharyya, J., S. Gross, J. Lees, and M. Hastings (1999), Recent earthquake sequences at Coso: Evidence for conjugate faulting and stress loading near a geothermal field, *Bull. Seismol. Soc. Am.*, *89*, 785–795.
- Blakely, R. J., R. C. Jachens, J. P. Calzia, and V. E. Langenheim (1999), Cenozoic basins of the Death Valley extended terrain as reflected in regional-scale gravity anomalies, in *Cenozoic Basins of the Death Valley Region*, edited by L. A. Wright and B. W. Troxel, *Spec. Pap. Geol. Soc. Am.*, *333*, 1–16.
- Cho, K. H., R. B. Herrmann, C. J. Ammon, and K. Lee (2007), Imaging the upper crust of the Korean Peninsula by surface-wave tomography, *Bull. Seismol. Soc. Am.*, *97*, 198–207, doi:10.1785/0120060096.
- Combs, J. (1980), Heat flow in the Coso geothermal area, Inyo County, California, *J. Geophys. Res.*, *85*, 2411–2424, doi:10.1029/JB085iB05p02411.
- Crafford, A. E. J. (2007), Geologic map of Nevada [CD-ROM], *U.S. Geol. Surv. Data Ser.*, *249*, 46 pp., scale 1:250,000. (Version 1.1 was released in 2008.)
- de Voogd, B., L. Serpa, L. Brown, E. Hauser, S. Kaufman, J. Oliver, B. W. Troxel, J. Willemin, and L.A. Wright (1986), Death Valley bright spot: A midcrustal magma body in the southern Great Basin, California?, *Geology*, *14*(1), 64–67, doi:10.1130/0091-7613(1986)14<64:DVBSAM>2.0.CO;2.
- Duffield, W. A., C. R. Bacon, and G. B. Dalrymple (1980), Late Cenozoic volcanism, geochronology, and structure of the Coso Range, Inyo County, California, *J. Geophys. Res.*, *85*, 2381–2404, doi:10.1029/JB085iB05p02381.
- Feng, Q., and J. M. Lees (1998), Microseismicity, stress, and fracture in the Coso geothermal field, California, *Tectonophysics*, *289*, 1–3, 221–238.
- Hauksson, E. (2000), Crustal structure and seismicity distribution adjacent to the Pacific and North America plate boundary in southern California, *J. Geophys. Res.*, *105*, 13,875–13,903, doi:10.1029/2000JB900016.
- Hauksson, E., and J. Unruh (2007), Regional tectonics of the Coso geothermal area along the intracontinental plate boundary in central eastern California: Three-dimensional V_p and V_p/V_s models, spatial-temporal seismicity patterns, and seismogenic deformation, *J. Geophys. Res.*, *112*, B06309, doi:10.1029/2006JB004721.
- Hough, S. E., J. M. Lees, and F. Monastero (1999), Attenuation and source properties at the Coso geothermal area, California, *Bull. Seismol. Soc. Am.*, *89*, 1606–1619.
- Jennings, C. W. (1977), Geologic map of California, *Geol. Data Map 2*, scale 1:750,000, Div. of Mines and Geol., Sacramento, Calif.
- Jones, C. H. (1987), Is extension in Death Valley accommodated by thinning of the mantle lithosphere beneath the Sierra Nevada, California?, *Tectonics*, *6*(4), 449–473, doi:10.1029/TC006i004p00449.
- Jones, C. H., and R. A. Phinney (1998), Seismic structure of the lithosphere from teleseismic converted arrivals observed at small arrays in the southern Sierra Nevada and vicinity, California, *J. Geophys. Res.*, *103*, 10,065–10,090, doi:10.1029/97JB03540.
- Lees, J. M., and H. Wu (2000), Poisson's ratio and porosity at Coso geothermal field, *J. Volcanol. Geotherm. Res.*, *95*, 157–173, doi:10.1016/S0377-0273(99)00126-2.
- Lin, F. C., M. H. Ritzwoller, J. Townend, S. Bannister, and M. K. Savage (2007), Ambient noise Rayleigh wave tomography of New Zealand, *Geophys. J. Int.*, *170*, 649–666, doi:10.1111/j.1365-246X.2007.03414.x.
- Lin, F. C., M. P. Moschetti, and M. H. Ritzwoller (2008), Surface wave tomography of the western United States from ambient seismic noise: Rayleigh and Love wave phase velocity maps, *Geophys. J. Int.*, *173*, 281–298, doi:10.1111/j.1365-246X.2008.03720.x.
- Lin, F. C., M. H. Ritzwoller, Y. Yang, M. P. Moschetti, and M. J. Fouch (2010), The stratification of seismic azimuthal anisotropy in the western US, *Nat. Geosci.*, *4*, 55–61, doi:10.1038/ngeo1036.
- Manley, C. R., and C. R. Bacon (2000), Rhyolite thermobarometry and the shallowing of the magma reservoir, Coso volcanic field, California, *J. Petrol.*, *41*, 149–174, doi:10.1093/petrology/41.1.149.
- McQuarrie, N., and M. Oskin (2010), Palinspastic restoration of NAVDat and implications for the origin of magmatism in southwestern North America, *J. Geophys. Res.*, *115*, B10401, doi:10.1029/2009JB006435.
- Monastero, F. C., A. Katzenstein, J. Miller, J. R. Unruh, M. Adams, and K. Richards-Dinger (2005), The Coso geothermal field: A nascent metamorphic core complex, *Geol. Soc. Am. Bull.*, *117*(11), 1534–1553, doi:10.1130/B25600.1.
- Moschetti, M. P., M. H. Ritzwoller, and N. M. Shapiro (2007), Surface wave tomography of the western United States from ambient seismic noise: Rayleigh wave group velocity maps, *Geochem. Geophys. Geosyst.*, *8*, Q08010, doi:10.1029/2007GC001655.
- Moschetti, M. P., M. H. Ritzwoller, and F. C. Lin (2010a), Seismic evidence for widespread crustal deformation caused by extension in the western USA, *Nature*, *464*(7290), 885–889, doi:10.1038/nature08951.
- Moschetti, M. P., M. H. Ritzwoller, F.-C. Lin, and Y. Yang (2010b), Crustal shear wave velocity structure of the western United States inferred from ambient seismic noise and earthquake data, *J. Geophys. Res.*, *115*, B10306, doi:10.1029/2010JB007448.
- Newman, G. A., E. Gasperikova, G. M. Hoversten, and P. E. Wannamaker (2008), Three-dimensional magnetotelluric characterization of the Coso geothermal field, *Geothermics*, *37*(4), 369–399, doi:10.1016/j.geothermics.2008.02.006.
- Nishida, K., H. Kawakatsu, and K. Obara (2008), Three-dimensional crustal S wave velocity structure in Japan using microseismic data recorded by Hi-net tiltmeters, *J. Geophys. Res.*, *113*, B10302, doi:10.1029/2007JB005395.
- Park, S. K., and B. Wernicke (2003), Electrical conductivity images of Quaternary faults and Tertiary detachments in the California Basin and Range, *Tectonics*, *22*(4), 1030, doi:10.1029/2001TC001324.
- Pluhar, C., R. S. Coe, J. C. Lewis, F. C. Monastero, and J. Glen (2006), Fault block kinematics at a releasing step-over of the Eastern California Shear Zone: Partitioning of rotation style in and around the Coso geothermal area and



- nascent metamorphic core complex, *Earth Planet. Sci. Lett.*, 250(1–2), 134–163, doi:10.1016/j.epsl.2006.07.034.
- Pullammanappalil, S., B. Honjas, J. Unruh, and F. Monastero (2001), Use of advance data processing techniques in the imaging of the Coso geothermal field, paper presented at 26th Workshop on Geothermal Reservoir Engineering, Stanford Univ., Stanford, Calif., 29–31 Jan.
- Pullammanappalil, S. K., and J. N. Louie (1993), Inversion of seismic reflection travel times using a nonlinear optimization scheme, *Geophysics*, 58(11), 1607–1620, doi:10.1190/1.1443376.
- Sabra, K. G., P. Gerstoft, P. Roux, W. A. Kuperman, and M. C. Fehler (2005), Surface wave tomography from microseism in southern California, *Geophys. Res. Lett.*, 32, L14311, doi:10.1029/2005GL023155.
- Saito, M. (1988), DISPER80: A subroutine package for the calculation of seismic normal-mode solution, in *Seismological Algorithms*, edited by D. J. Doornbos, pp. 293–319, Elsevier, New York.
- Saltus, R. W., and A. H. Lachenbruch (1991), Thermal evolution of the Sierra Nevada: Tectonic implications of new heat flow data, *Tectonics*, 10(2), 325–344, doi:10.1029/90TC02681.
- Sanders, C., P. Ho-Liu, D. Rinn, and H. Kanamori (1988), Anomalous Shear-Wave Attenuation in the Shallow Crust Beneath the Coso Volcanic Region, California, *J. Geophys. Res.*, 93, 3321–3338, doi:10.1029/JB093iB04p03321.
- Saygin, E., and L. N. Kennett (2010), Ambient seismic noise tomography of Australian continent, *Tectonophysics*, 481, 116–125, doi:10.1016/j.tecto.2008.11.013.
- Shapiro, N. M., M. Campillo, L. Stehly, and M. H. Ritzwoller (2005), High-resolution surface wave tomography from ambient seismic noise, *Science*, 307(5715), 1615–1618, doi:10.1126/science.1108339.
- Taylor, T. R., J. F. Dewey, and F. C. Monastero (2008), Trans-tensional deformation of the brittle crust: Field observations and theoretical applications in the Coso-China lake region, Eastern margin of the Sierra Nevada microplate, southeastern California, *Int. Geol. Rev.*, 50(3), 218–244, doi:10.2747/0020-6814.50.3.218.
- Tsai, V. C., and M. P. Moschetti (2010), An explicit relationship between time-domain noise correlation and spatial auto-correlation (SPAC) results, *Geophys. J. Int.*, 182, 454–460, doi:10.1111/j.1365-246X.2010.04633.x.
- Unruh, J. R., F. C. Monastero, and S. K. Pullammanappalil (2008), The nascent Coso metamorphic core complex, east-central California: Brittle upper plate structure revealed by reflection seismic data, *Int. Geol. Rev.*, 50(3), 245–269, doi:10.2747/0020-6814.50.3.245.
- Villaseñor, A., Y. Yang, M. H. Ritzwoller, and J. Gallart (2007), Ambient noise surface wave tomography of the Iberian Peninsula: Implications for shallow seismic structure, *Geophys. Res. Lett.*, 34, L11304, doi:10.1029/2007GL030164.
- Walck, M. C. (1988), Three-dimensional V_p/V_s for the Coso region, California, *J. Geophys. Res.*, 93, 2047–2052, doi:10.1029/JB093iB03p02047.
- Walck, M. C., and R. W. Clayton (1987), P wave velocity variations in the Coso region, California, derived from local earthquake travel times, *J. Geophys. Res.*, 92, 393–405, doi:10.1029/JB092iB01p00393.
- Wernicke, B. (1985), Uniform-sense normal simple shear of the continental lithosphere, *Can. J. Earth Sci.*, 22, 108–125, doi:10.1139/e85-009.
- Wilson, C. K., C. H. Jones, and H. J. Gilbert (2003), A single-chamber silicic magma system inferred from shear-wave discontinuities of the crust and uppermost mantle, Coso geothermal area, California, *J. Geophys. Res.*, 108(B5), 2226, doi:10.1029/2002JB001798.
- Wu, H., and J. M. Lees (1996), Attenuation structure of Coso geothermal area, California, from wave pulse widths, *Bull. Seismol. Soc. Am.*, 86, 1574–1590.
- Wu, H., and J. M. Lees (1999), Three-dimensional P and S velocity structures of the Coso geothermal area, California, from microseismic travel-time data, *J. Geophys. Res.*, 104, 13,217–13,233, doi:10.1029/1998JB900101.
- Yang, Y., M. Ritzwoller, A. Levshin, and N. Shapiro (2007), Ambient noise rayleigh wave tomography across Europe, *Geophys. J. Int.*, 168, 259–274, doi:10.1111/j.1365-246X.2006.03203.x.
- Yang, Y. J., A. B. Li, and M. H. Ritzwoller (2008a), Crustal and uppermost mantle structure in southern Africa revealed from ambient noise and teleseismic tomography, *Geophys. J. Int.*, 174, 235–248, doi:10.1111/j.1365-246X.2008.03779.x.
- Yang, Y. J., M. H. Ritzwoller, F. C. Lin, M. P. Moschetti, and N. M. Shapiro (2008b), Structure of the crust and uppermost mantle beneath the western United States revealed by ambient noise and earthquake tomography, *J. Geophys. Res.*, 113, B12310, doi:10.1029/2008JB005833.
- Yang, Y., et al. (2010), Rayleigh wave phase velocity maps of Tibet and the surrounding regions from ambient seismic noise tomography, *Geochem. Geophys. Geosyst.*, 11, Q08010, doi:10.1029/2010GC003119.
- Yao, H., R. D. van der Hilst, and M. V. de Hoop (2006), Surface-wave array tomography in SE Tibet from ambient seismic noise and two-station analysis—I. Phase velocity maps, *Geophys. J. Int.*, 166, 732–744, doi:10.1111/j.1365-246X.2006.03028.x.
- Young, C., and R. W. Ward (1980), Three-dimensional Q^{-1} model of the Coso Hot Springs known geothermal resource, *J. Geophys. Res.*, 85, 2459–2470, doi:10.1029/JB085iB05p02459.
- Zheng, S. H., X. L. Sun, X. D. Song, Y. J. Yang, and M. H. Ritzwoller (2008), Surface wave tomography of China from ambient seismic noise correlation, *Geochem. Geophys. Geosyst.*, 9, Q05020, doi:10.1029/2008GC001981.